ISSN (Print) 1226-1750
ISSN (Online) 2233-6656
Journal of Magnetics 31(3), 365-375 (2026) https://doi.org/10.4283/JMAG.2026.31.3.365

SAR and Temperature Analysis of Dental Implants for UHF-MRI RF Safety: Simulation Study

Eunwoo Lee[1], Kyoung-Nam Kim[2], Jae-Young Kim[3], Ji-Youn Kim[4]*, and Young-Eun Kwon[5]*

[1]Gachon Biomedical Convergence Institute, Gachon University Gil Medical Center, Namdong-daero 774beon-gil, Namdong-gu, Incheon 21565, Republic of Korea
[2]Department of Biomedical Engineering, Gachon University, 1342, Seongnam-daero, Sujeong-gu, Seongnam-si, Gyeonggi-do 13120, Republic of Korea
[3]Department of Biochemistry, School of Dentistry, IHBR, Kyungpook National University, 2177, Dalgubeol-daero, Jung-gu, Daegu 41940, Republic of Korea
[4]Department of Dental Hygiene, Gachon University, 191, Hambangmoe-ro, Yeonsu-gu, Incheon 21936, Republic of Korea
[5]Department of Oral and Maxillofacial Radiology, School of Dentistry, IHBR, Kyungpook National University, 2177, Dalgubeol-daero, Jung-gu, Daegu 41940, Republic of Korea

(Received 15 May 2026, Received in final form 28 July 2026, Accepted 29 July 2026)

This study used numerical simulations to examine specific absorption rate (SAR) distribution and temperature changes caused by radiofrequency (RF) exposure in 3T and 11.74T MRI environments for patients with dental implants. Five scenarios with different implant numbers and placements were analyzed. In the 3T environment, whole-head average temperature increases stayed below 0.5°C in all cases, complying with safety guidelines. Local temperatures in the dental region reached approximately 43°C regardless of implant presence, with implants producing only marginal differences in localized heating patterns. In the 11.74T environment, dental region temperatures exceeded 46°C within 15 minutes in all cases including the implant-free baseline, primarily due to the higher input power required to achieve the normalized whole-body SAR limit at ultra-high field strength. While single-voxel peak SAR values near implants showed some elevation at 11.74T, these differences became negligible when averaged over 1 g or 10 g tissue mass. The elevated temperatures at 11.74T were predominantly driven by the normalization-imposed input power rather than implant-induced field enhancement. Nevertheless, implant configuration significantly influenced the spatial distribution and localization of heating, with implications for clinical MRI safety protocols in ultra-high-field environments.

Keywords : magnetic resonance imaging, specific absorption rate, dental implant, electromagnetic field, radiofrequency

1. Introduction

Magnetic resonance imaging (MRI) is widely used in both research and clinical practice because it provides high-resolution images with excellent soft tissue contrast [1–4]. In particular, ultra-high-field MRI at 7T and above is valuable for visualizing fine brain structures and investigating neurological diseases, owing to its superior signal-to-noise ratio and spatial resolution compared with 1.5T and 3T systems. However, ultra-high-field MRI may pose safety concerns, including inhomogeneous electric-field distributions within the human body and tissue heating caused by radiofrequency (RF) energy deposition. These effects result from strong static magnetic fields and high-frequency electromagnetic fields involved [5, 6]. Because direct measurement of internal electric fields in the human body is not feasible in practice, a common approach is to compute electromagnetic field distributions within high-resolution anatomical human body models using numerical methods based on Maxwell's equations. These simulations are then used to calculate the specific absorption rate (SAR), a key metric for assessing human safety with respect to RF exposure [7, 8].

As the demand for MRI examinations among patients

©The Korean Magnetics Society. All rights reserved.
*Co-corresponding author: Tel: +82-32-820-4376,
Fax: +82-32-820-4449, E-mail: hoho6434@gachon.ac.kr (Ji-Youn Kim)
Tel: +82-53-600-7424, Fax: +82-53-425-6025
E-mail: yekwon@knu.ac.kr (Young-Eun Kwon)

with implantable medical devices has grown in recent years, the importance of MRI safety evaluation for passive implantable medical devices (PIMDs) has increased. Assessing the MRI safety of PIMDs requires consideration of several risk factors, including magnetically induced mechanical hazards (force and torque), RF-induced heating, image artifacts, and MR conditional labeling. With respect to RF-induced heating, extensive numerical and experimental studies have been conducted on various PIMDs in 1.5T and 3T MRI environments. In addition, the RF safety of small metallic devices, such as aneurysm clips and dental implants, has been partially reported in the context of 7T head MRI [9–12]. Metallic PIMDs, including dental implants, can interact with strong electromagnetic fields during MR scanning, inducing localized power deposition and temperature elevation in the tissue surrounding the implant. As the magnetic field strength increases, the RF wavelength decreases, altering resonance conditions relative to implant dimensions and potentially resulting in wave interference and localized power concentrations (hot spots). Furthermore, the worst-case dimensions of implantable medical devices are determined by the RF wavelength, with reports indicating that maximum heating occurs in implants with lengths of approximately half the RF wavelength, suggesting that heating characteristics may vary with field strength [9, 13, 14].

In light of these considerations, this study analyzed the changes in SAR and temperature elevation associated with the presence or absence of dental implants in 3T and 11.74T MRI environments using electromagnetic field simulations. It also evaluated the feasibility of establishing MR Conditional status under ultra-high-field conditions. Specifically, numerical simulations were performed to evaluate RF-induced heating near the implant, following ASTM F2182-19e2—a standard test method established by the American Society for Testing and Materials (ASTM) that specifies the experimental and computational procedures for assessing RF-induced heating of passive implants during MRI [15]. Field strength, implant presence or absence, number of implants, and implant placement were treated as variables, enabling a systematic assessment of the RF safety of dental implants in ultra-high-field MRI environments.

2. Materials and Methods

2.1. Electromagnetic Simulation Set-up

Electromagnetic field simulations were performed using Sim4Life 7.2.3 (Zurich MedTech, Zurich, Switzerland: https://www.zmt.swiss). Sim4Life is a comprehensive computational life sciences simulation platform with specialized modules for MRI implant safety assessment, enabling evaluation of interactions between RF radiation and medical implants within anatomical models. The finite-difference time-domain (FDTD) method was used for electromagnetic field analysis.

As shown in Fig. 1(a), the RF coil for the 3T MRI system was modeled as a 16-leg high-pass birdcage coil based on the standard bore diameter of 700 mm commonly used in clinical settings [16]. The coil dimensions were 700 mm in diameter, 480 mm in height, and 40 mm in conductor width, and it was tuned to the Larmor frequency of 128 MHz. The conductors were set as perfect

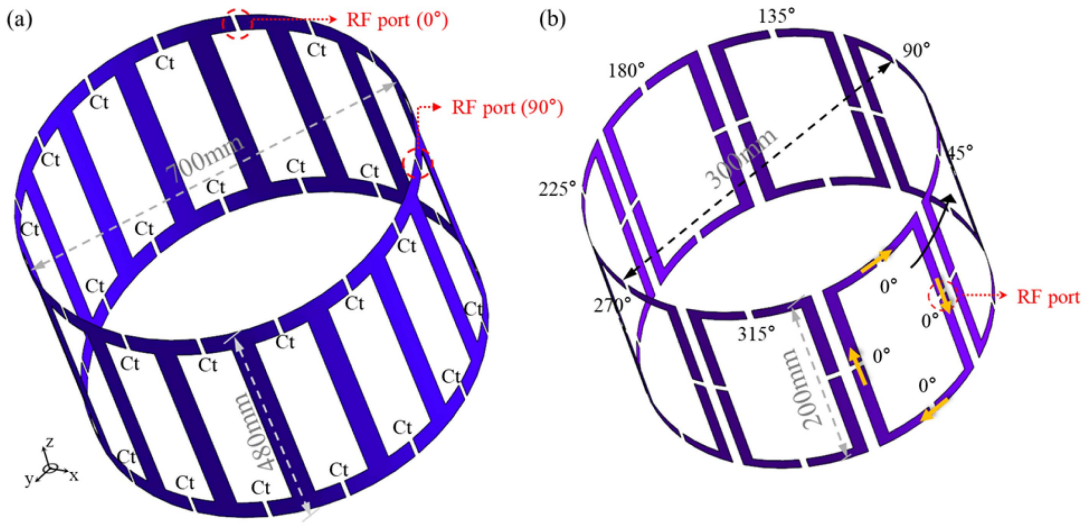


Fig. 1. (Color online) Radiofrequency (RF) coil models used in electromagnetic field simulations. (a) 16-leg high-pass birdcage coil for 3T magnetic resonance imaging (MRI) system; (b) 8-channel loop coil array for 11.74T MRI system.

electric conductors (PEC), and the tuning capacitor value was set to 25.45 pF. Phase angles of 0° and 90° were applied to the two RF ports to enable circular polarization (CP) mode operation. The validity of the modeled birdcage coil was verified by comparing the $|B_1^+|$ distribution with that obtained from a CP-mode Huygens-equivalent source generated from the same coil structure.

The Larmor frequency of the 11.74T MRI system is approximately 500 MHz. Because no standardized commercial coil currently exists for this field strength, an 8-channel loop coil array commonly employed in ultra-high-field MRI research was modeled (Fig. 1(b)) [17]. The conductor width of each loop coil was 10 mm, and the coils were evenly distributed at 45° intervals on the surface of a cylindrical housing with a diameter of 300 mm and a height of 200 mm. The conductors were also modeled as PEC, consistent with the 3T coil configuration. The coil was driven in CP mode with a 45° phase difference between adjacent channels, and a current of 4 A was applied to each channel.

The human body model used in this study was the adult male model (Duke, 34 years old) provided by the IT'IS Foundation Virtual Population V3.0 [18]. The brain was defined as the region of interest, and the human body model was positioned such that the thalamus, representing the central region of the brain, was aligned with the isocenter of each coil.

A MEGAGEN dental implant (diameter: 4.5 mm; height: 10 mm) was used as the reference model for implant design. Fig. 2(a) illustrates that the human body model used in the electromagnetic field simulations included 28 teeth, excluding the third molars. In this study, the second premolar and first molar in the posterior region were selected as implant insertion sites. As shown in Fig. 2(b), the implant model consisted of four components: crown, gingiva, abutment, and fixture. The electrical properties of each component were assigned based on the material database in Sim4Life and materials commonly used in clinical practice. Specifically, the crown was set as ceramic and the gingiva as mucous

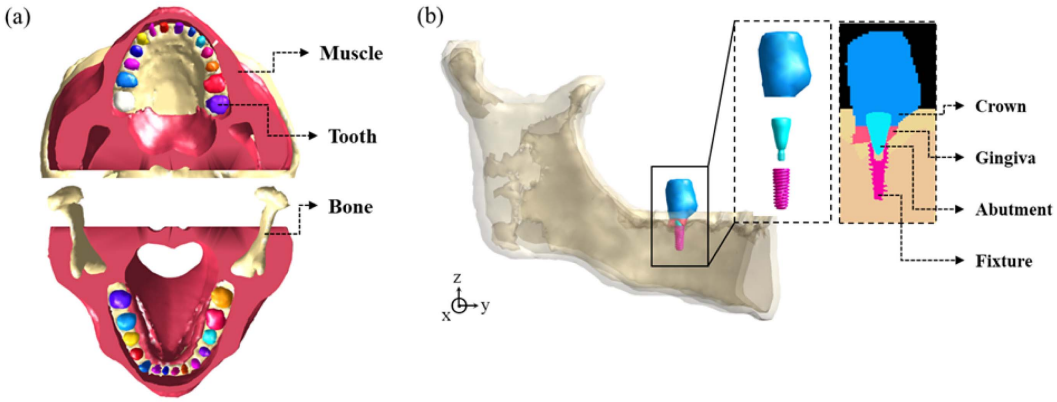


Fig. 2. (Color online) Dental and implant models used in electromagnetic field simulations. (a) Intraoral tooth placement configuration of the IT'IS Foundation Virtual Population V3.0 Duke human body model; (b) Components of the dental implant model (crown, gingiva, abutment, and fixture).

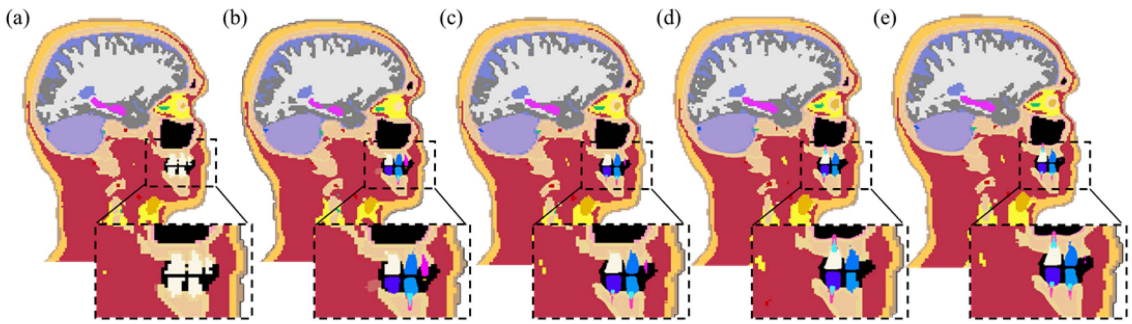


Fig. 3. (Color online) Five simulation cases according to implant placement conditions. (a) Baseline Duke model without implants; (b) Single implant placed in the right mandibular molar region; (c) Two adjacent implants placed in the right mandibular molar region; (d) One implant each placed in opposing positions in the right maxillary and mandibular molar regions; (e) Three adjacent implants placed in the right molar region.

membrane, whereas the abutment and fixture were set as PEC [9–11]. Each implant was positioned in the posterior region of the mouth based on actual clinical cases.

To evaluate the effects of implant position and quantity on RF-induced heating, a total of five simulation cases were configured (Fig. 3): (1) the baseline Duke model without implants (Fig. 3(a)); (2) a single implant placed in the right mandibular molar region (Fig. 3(b)); (3) two adjacent implants placed in the right mandibular molar region (Fig. 3(c)); (4) one implant each placed in opposing positions in the right maxillary and mandibular molar regions (Fig. 3(d)); and (5) three adjacent implants placed in the right molar region (Fig. 3(e)).

For accurate electromagnetic field and thermal analysis, the maximum voxel size of the Duke human body model was set to 2 × 2 × 2 mm³. In the implant region, finer discretization was applied to accurately preserve the sub-millimeter structural features of the metallic components: the abutment and fixture were refined to a resolution of 0.1 × 0.1 × 0.1 mm³, while the crown and gingiva were set to 0.3 × 0.3 × 0.3 mm³. This multi-resolution configuration was selected to preserve the fine geometric features of the dental implant components without staircasing distortion, while maintaining computational tractability. This refinement is critical not only for spatial resolution but also for the accurate computation of local SAR, as electromagnetic field enhancements near metallic implant surfaces are highly sensitive to voxel discretization. Further refinement of the voxel size would lead to an exponential increase in computational time, particularly for the thermal simulations, making such simulations impractical with available resources. The total number of voxels in the computational grid, depending on implant presence, quantity, and position, ranged from approximately 89.35 to 142.64 mega-cells for the 3T simulations and from approximately 51.86 to 136.84 mega-cells for the 11.74T simulations.

2.2. Specific Absorption Rate Analysis

For RF safety evaluation, the local SAR within the human body and the SAR averaged over 1 g or 10 g of tissue (SAR_{1g}, SAR_{10g}) were calculated using Equations (1) and (2), respectively.

$$SAR(r) = \frac{\sigma}{2\rho} E^2 \tag{1}$$

$$(SAR)_M = \frac{1}{M} \int_{R(M)} SAR(r)\, dm \tag{2}$$

In Eq. (1), r denotes an arbitrary spatial coordinate (x, y, z), E represents the induced electric field, and ρ denotes tissue density. In Eq. (2), M represents the mass within the integration region R, and V denotes the corresponding volume. To limit SAR in accordance with the International Electrotechnical Commission (IEC) guidelines (Table 1), the head average SAR (hdSAR), peak-spatial 1 g-averaged SAR ($psSAR_{1g}$), peak-spatial 10 g-averaged SAR ($psSAR_{10g}$), and whole-body average SAR (wbSAR) were calculated to evaluate RF safety [19].

To quantitatively compare the simulation results between 3T and 11.74T, the RF coil configurations were selected to reflect the most widely adopted designs at each field strength: a birdcage body coil at 3T and an 8-channel transmit loop coil array at 11.74T. Because these coil architectures exhibit fundamentally different $|B_1^+|$ generation efficiencies, comparing SAR at an identical input power would not constitute a physically equitable comparison. Therefore, we adopted the following peak $|B_1^+|$ value normalization procedure to enable a fair comparison: (i) Simulations were conducted at a normalized input power of 1 W for both field strengths, yielding a maximum $|B_1^+|$ of 1.74 μT at 3T and 0.32 μT at 11.74T. The 3T maximum $|B_1^+|$ (approximately 1.7 μT) was defined as the reference level. (ii) Given the linear relationship between $|B_1^+|$ and $\sqrt{P}$, the input power at 11.74T was scaled to 28.5 W to match this reference level. (iii) Under the matched peak $|B_1^+|$ values, wbSAR, hdSAR, $psSAR_{1g}$, and $psSAR_{10g}$ were computed for both field strengths. (iv) The resulting SAR values were then compared against the IEC guideline normal operating mode limits, across field strengths (3T versus 11.74T), and within each field strength between implant-free and implant-included conditions.

Table 1. IEC SAR limitation criteria for MRI scanning.

Mode	Whole body SAR (W/kg)	Partial SAR (W/kg)	head SAR (W/kg)	local SAR (W/kg)		
				head	abdomen	extreme
Normal	2	2–10	3.2	10	10	20
First control	4	4–10	3.2	20	20	40
Second control	> 4	> (4–10)	> 3.2	> 20	> 20	> 40

Abbreviations: IEC, International Electrotechnical Commission; SAR, specific absorption rate; MRI, magnetic resonance imaging.

2.3. Temperature Analysis

In the thermal simulation, temperature changes in the human body model due to RF power exposure were calculated using the thermal analysis solver in Sim4Life, based on the Pennes bioheat equation (Eq. (3)).

$$\rho c\frac{\partial T}{\partial t} = \nabla\cdot\left(k\nabla T\right) + \rho Q + \rho SAR - \rho_b c_b \rho_\omega \left(T - T_b\right) \quad (3)$$

Here, k denotes thermal conductivity, ρ denotes tissue density, Q represents the metabolic heat generation rate, and ω represents the blood perfusion rate, whereas ρ_b, c_b, and T_b denote the density, specific heat capacity, and temperature of blood, respectively. Since blood circulating rapidly throughout the body is assumed to maintain a uniform temperature via thermoregulatory mechanisms, blood temperature was set to a fixed value in the Pennes bioheat equation calculations.

The initial temperature of all tissues in the human body model was set to 37 °C, and after reaching a stable thermal equilibrium through heat exchange with the external environment (temperature: 22 °C, heat transfer coefficient: 8 W/(m²·K)), a simulation was performed in which RF power was applied for a total of 15 minutes [20].

The RF power applied during the thermal simulation was normalized to the maximum power satisfying the wbSAR limit of 2 W/kg under the Normal Operating Mode of the IEC guidelines. Accordingly, a power of 22.6 W was applied across all cases in the 3T environment, regardless of implant presence or quantity, whereas in the 11.74T environment, the applicable power differed by case (Table 2).

The thermal properties of the implant components (abutment and fixture) used in the thermal simulation were set as follows: mass density of 4400 kg/m³, specific heat capacity of 550 J/(kg·K), and thermal conductivity of 7.2 W/(m·K) [9].

The thermal simulation results were used to evaluate temperature changes in the head region of the human body model based on the temperature safety criteria for the Normal Operating Mode specified in IEC 60601-2-33. These criteria include a maximum core body temperature increase of 0.5 °C and local tissue temperature limits (head: 38 °C; torso: 39 °C; extremities: 40 °C). Additionally, to analyze the implant sub-regions in detail, the maximum temperature values across the entire dental region of the Duke model were extracted, and temporal temperature variations were analyzed.

3. Results

3.1. Electromagnetic Simulation

Table 3 presents the SAR results for each case, normalized to a comparable maximum $|B_1^+|$-field value (approximately 1.7 μT). In the field-strength comparison, the SAR values at 11.74T were higher than those at 3T across all cases, regardless of implant presence. Compared with 3T, wbSAR, hdSAR, $psSAR_{1g}$, and $psSAR_{10g}$

Table 2. Maximum applicable input power for each case satisfying the wbSAR limit of 2 W/kg for MRI scanning.

		Case 1	Case 2	Case 3	Case 4	Case 5
3T	Total Power (W)	22.6	22.6	22.6	22.6	22.6
11.74T	Total Power (W)	430.2	429.6	429.1	427.3	426.8

Abbreviations: wbSAR, whole-body specific absorption rate; SAR, specific absorption rate; MRI, magnetic resonance imaging.

Table 3. SAR simulation results for each case in the 3T (normalized to 1 W) and 11.74T (normalized to 28.5 W) environments. (Case 1: no implant, Case 2: single implant in mandibular molar region, Case 3: two adjacent implants in mandibular molar region, Case 4: two opposing implants in maxillary and mandibular molar regions, Case 5: three adjacent implants in molar region).

		Case 1	Case 2	Case 3	Case 4	Case 5
3T (1W) (W/kg/W)	wbSAR	0.088	0.088	0.088	0.088	0.088
	hdSAR	0.591	0.593	0.593	0.593	0.593
	$psSAR_{10g}$	1.674	1.668	1.666	1.686	1.685
	$psSAR_{1g}$	2.930	2.844	2.843	2.912	2.823
11.74T (28.5W) (W/kg/W)	wbSAR	0.133	0.133	0.133	0.133	0.134
	hdSAR	1.469	1.473	1.475	1.481	1.484
	$psSAR_{10g}$	4.446	4.472	4.483	4.369	4.403
	$psSAR_{1g}$	6.962	7.005	7.029	7.047	7.081

Abbreviations: SAR, specific absorption rate.

at 11.74T increased within ranges of 49.87~51.28%, 148.34~150.45%, 137.61~150.83%, and 159.15~169.16%, respectively. While $psSAR_{10g}$ is the regulatory metric specified by IEC 60601-2-33, $psSAR_{1g}$ was additionally evaluated to capture potential localized SAR enhancement near the metallic implant surfaces that may be attenuated by 10 g tissue averaging.

In the evaluation against the IEC 60601-2-33 Normal Operating Mode limits, the 3T environment (normalized to 1 W) showed wbSAR at approximately 4.4% of the limit (2 W/kg), hdSAR at approximately 18.5% of the limit (3.2 W/kg), and $psSAR_{10g}$ at approximately 16.7% of the limit (10 W/kg), all of which were confirmed to be substantially below the limits across all cases regardless of implant presence. In the 11.74T environment (normalized to 28.5 W), wbSAR, hdSAR, and $psSAR_{10g}$ were approximately 6.6%, 46.0%, and 44.0% of their respective limits, respectively. All values remained below the prescribed limits across all cases; however, they were relatively closer to the limits than those observed at 3T.

In the comparison based on implant presence, SAR changes attributable to implants within the same field strength were found to be negligible. In the 3T environment, wbSAR decreased by approximately 0.1%, hdSAR increased by approximately 0.3%, and $psSAR_{10g}$ varied within a range of -0.5% to 0.7% relative to the implant-free condition. In the 11.74T environment, wbSAR increased by approximately 0.1~0.7% and hdSAR by approximately 0.2~0.9%, while $psSAR_{10g}$ varied within a range of -1.0% to 0.8%.

Figures 4 and 5 illustrate the $|B_1^+|$-field, |E|-field, and local SAR maps around the implants for each case in the 3T and 11.74T environments, respectively. Panel (a) in each figure shows the distributions under the implant-free conditions, while panels (b)–(e) show the sagittal plane distributions centered on the implant locations.

In the 3T environment, distortion of the $|B_1^+|$-field was observed in regions where implants were present, and the |E|-field in the same sagittal plane showed a locally elevated electric field near the edges of the implants.

In the 11.74T environment, distortion of the $|B_1^+|$-field and elevation of the electric field at the implant edges were similar to those observed in the 3T case. However, unlike in the 3T environment, the local SAR map showed a pronounced increase in SAR values in regions with implants. In particular, in cases involving two or more implants, the maximum local SAR occurred at the implant edges. Nevertheless, when SAR was evaluated by averaging over a 1 g or 10 g volume, the localized SAR elevation was mitigated because the implant volume was considerably smaller than the averaging volume, and no significant SAR changes attributable to the implants were observed.

3.2. Temperature Simulation

Figures 6 and 7 show temperature variations for each

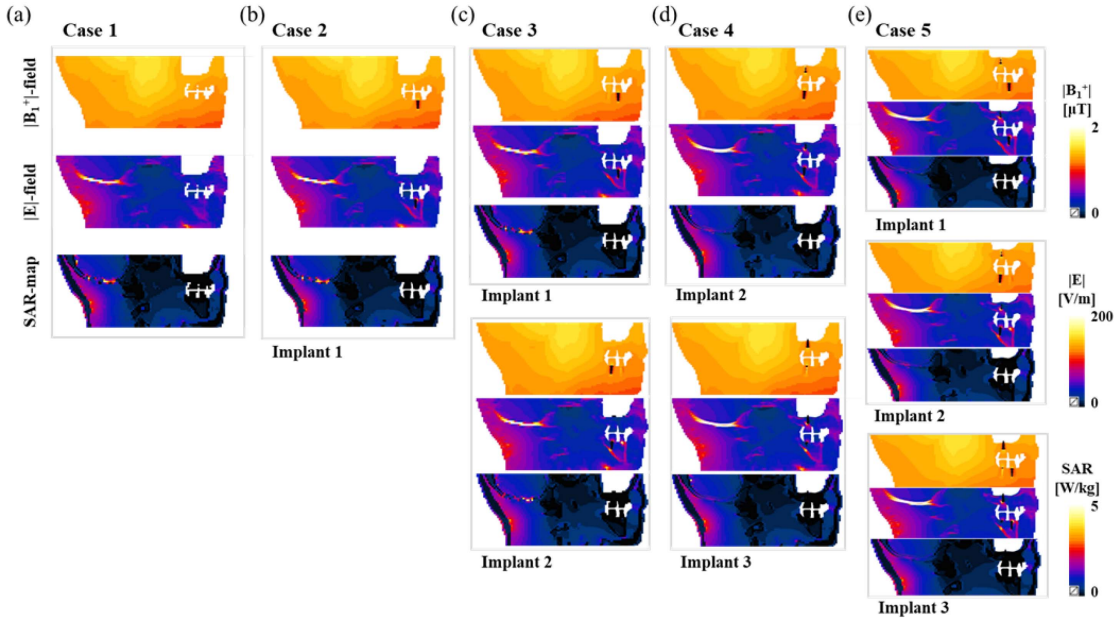


Fig. 4. (Color online) Sagittal distributions of $|B_1^+|$-field, |E|-field, and local specific absorption rate (SAR) maps for each case in the 3T environment. The sagittal plane represents the central sagittal view of each implant location within up to three individual cases, enabling comparison of electromagnetic field distributions and local SAR variations around implants.

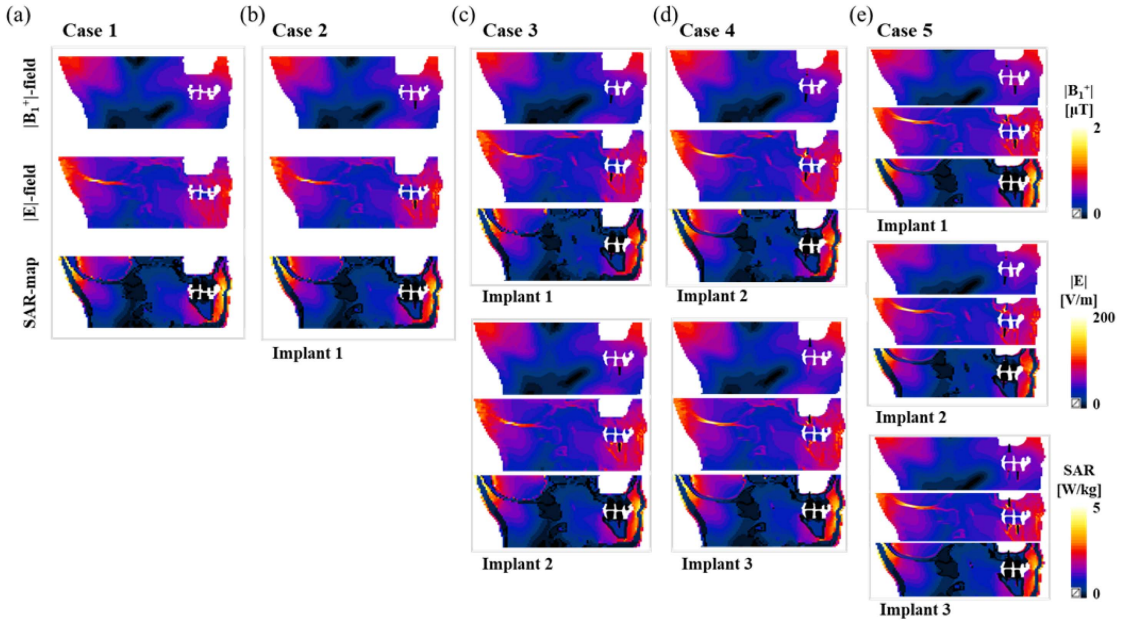


Fig. 5. (Color online) Sagittal distributions of $|B_1^+|$-field, |E|-field, and local specific absorption rate (SAR) maps for each case in the 11.74T environment. The sagittal plane provides a central sagittal view of each implant location within up to three individual cases, enabling comparison of electromagnetic field distributions and local SAR variations around implants.

case during 15 minutes of exposure at the RF power corresponding to the wbSAR safety limit, where (a) corresponds to the 3T environment and (b) to the 11.74T environment. Fig. 6 shows the temperature variation at the center of the head, and Fig. 7 shows the maximum temperature variation in the dental region. Analysis of the average temperature variation in the head region revealed that, in the 3T environment, the temperature rise remained within 0.5 °C during 15 minutes of RF exposure, regardless of implant presence or placement configuration, and no temperature rise exceeding the permissible limit of the IEC guideline Normal Operating Mode was observed. In the 11.74T environment, however, the temperature rose sharply within approximately 3 minutes of exposure onset and subsequently converged to around 39 °C. No notable temperature differences attributable to the number or placement of implants were observed.

Analysis of the maximum temperature variation within the dental region revealed different patterns across cases in the 3T environment. In the absence of implants (Case

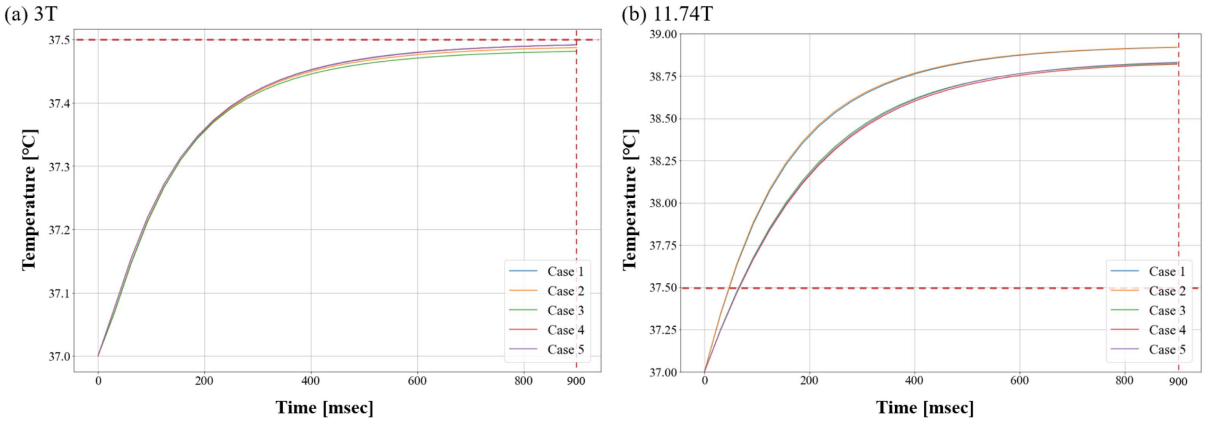


Fig. 6. (Color online) Maximum temperature variation in the dental region of the human body model according to magnetic field strength.

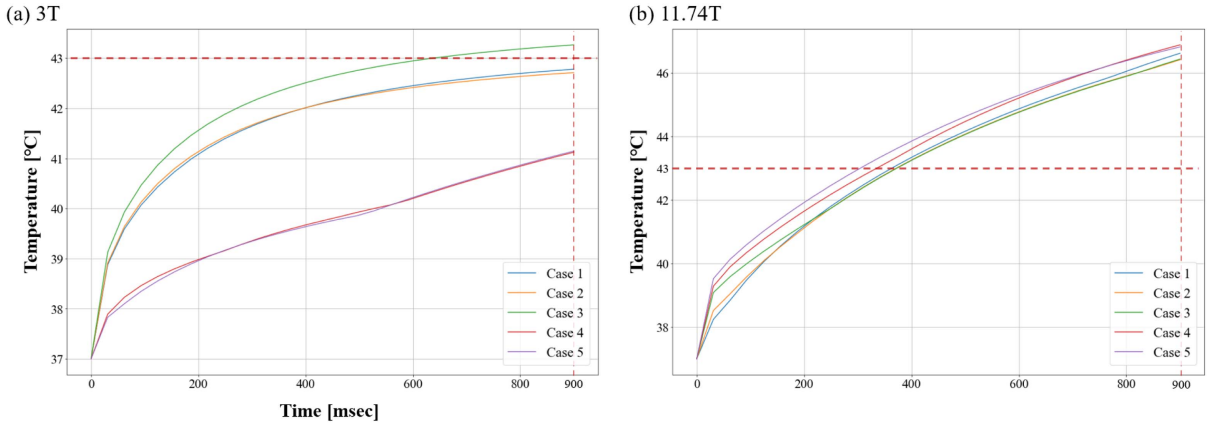


Fig. 7. (Color online) Temperature variation at the center of the head of the human body model according to magnetic field strength.

1), with a single implant (Case 2), and with implants placed adjacently in the mandibular molar region (Case 3), the temperature tended to converge to approximately 43 °C over time. In contrast, in cases involving implants placed in opposing positions in the maxillary and mandibular regions (Cases 4 and 5), the temperature reached after 15 minutes was relatively lower at approximately 41 °C; however, after 7 minutes, the temperature did not converge to a specific value but instead showed a linearly increasing trend over time. In the 11.74T environment, the maximum temperature exceeded 46 °C after 15 minutes of exposure, regardless of implant presence, quantity, or placement, and a linear increase over time was observed across all cases.

Figure 8 shows the sagittal temperature distributions after 15 minutes of exposure at the RF power corresponding to the wbSAR safety limit for each case. The sagittal plane position was set to a cross-section of the region commonly included in cases with implants to compare temperature changes by implant presence. In the 3T environment, overall changes in temperature distribution were minimal, and no localized temperature differences attributable to implant presence were observed. In the 11.74T environment, a generally higher and more uniform temperature distribution was observed compared with the 3T environment; however, no abrupt temperature rise or localized heat concentration in the regions surrounding the implants was evident. This is consistent with the previously analyzed SAR results and suggests that localized SAR elevation caused by the implants is mitigated in the temperature distribution by thermal diffusion.

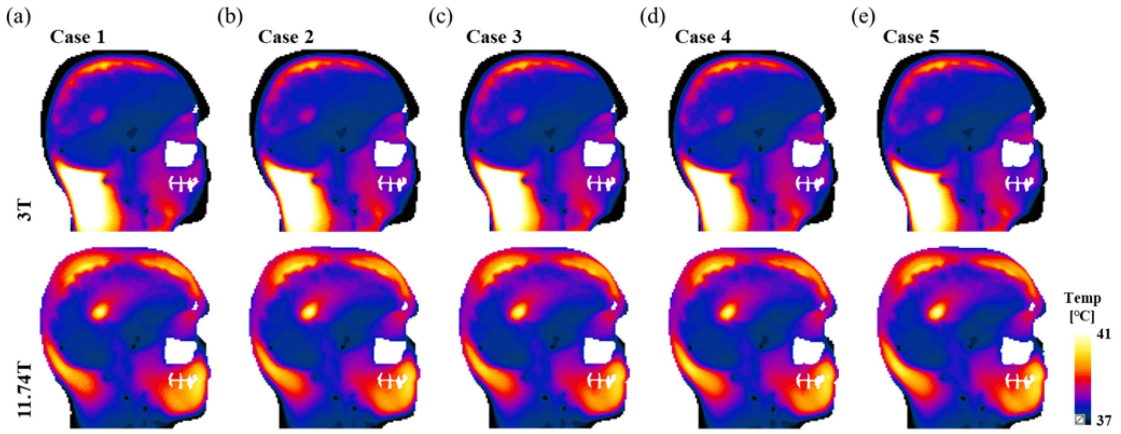


Fig. 8. (Color online) Sagittal temperature distributions of the human body model after 15 minutes of radiofrequency (RF) exposure according to magnetic field strength and implant placement conditions. (Top) 3T; (Bottom) 11.74T.

4. Discussion

In this study, the SAR distribution and temperature variations induced by RF electromagnetic field exposure in 3T and 11.74T MRI environments were systematically analyzed using numerical simulations in patients with dental implants. Five simulation scenarios with varying implant presence, quantity, and placement were defined to quantitatively evaluate the effects of implant configuration on the thermal response of the human body. As a simulation-based parametric study, the primary objective was to identify potential thermal risk patterns across various implant configurations using a validated commercial simulation tool; experimental validation through ASTM F2182 phantom measurements remains a valuable next step, particularly at 11.74T where no standardized protocol currently exists for ultra-high-field implant safety assessment.

4.1. Electromagnetic Simulation

The simulation results showed that distortion of the surrounding electromagnetic field due to the presence of the metallic implants, modeled as a perfect electric conductor (PEC) to represent the titanium implant, was commonly observed in both the 3T and 11.74T MRI environments [9]. In the 3T case, localized SAR concentration in the tissues surrounding the implants was not prominent. Specifically, analysis of the local SAR map revealed no notable changes or distortions in SAR values, likely due to the influence of the electrical properties of the tissues surrounding the implants. In contrast, in the 11.74T case, a more pronounced localized SAR concentration was observed. However, this localized increase in SAR remained within regulatory limits when averaged over 1 g or 10 g units. This finding indicates that subtle electromagnetic field distortion around the implants does not abruptly increase the average thermal load in the tissue, suggesting that the practical risk of thermal damage from localized SAR peaks is relatively low.

The implant components (abutment and fixture) were modeled as a perfect electric conductor (PEC). Although dental implants are physically manufactured from titanium, the use of PEC is a standard and well-established approximation in RF electromagnetic simulations of metallic implants. This is because the RF skin depth of titanium ($\sigma \approx 1.8\times10^6$ S/m) is only about 33 μm at 128 MHz (3T) and 17 μm at 500 MHz (11.74T), which is far smaller than the millimeter-scale dimensions of the implant. Consequently, the RF currents are confined to a thin surface layer, and the resulting surface current distribution, which governs the surrounding field and local tissue heating, is essentially identical to that of a PEC.

Furthermore, the localized elevation in SAR did not directly translate into a corresponding localized temperature concentration. This behavior can be attributed to the combined effects of thermal diffusion within biological tissues and the heat-dissipation effect of blood flow, which together sufficiently dispersed heat to prevent the formation of distinct thermal hot spots in the temperature distribution, despite localized SAR elevations around the implants.

4.2. Temperature Simulation

The thermal simulation results in the 3T MRI environment showed that the average temperature rise across the entire head region remained within 0.5 °C in all cases, thereby satisfying the permissible temperature rise criteria specified under the Normal Operating Mode of the IEC guidelines. Additionally, the differences in the average temperature rise across the entire head region according to implant presence and quantity (Cases 1 through 3) were small, remaining within 0.1 °C, indicating that the implants had a limited effect on the systemic thermal load in the 3T environment.

However, when local temperatures were analyzed specifically within the dental region, different patterns were observed. Notably, the 15-minute exposure adopted in this study follows the standard reference period of the IEC 60601-2-33 guideline, as our objective was to assess compliance with this safety criterion rather than to characterize the long-term asymptotic thermal behavior. In cases 2 and 3, the maximum temperature in the dental region tended to converge at approximately 43 °C. Since 43 °C is close to the threshold temperature at which thermal denaturation of cellular proteins begins, the possibility of localized tissue damage upon prolonged exposure cannot be excluded. Notably, in cases involving implants placed in opposing positions in the maxillary and mandibular regions (Cases 4 and 5), the temperature in the dental region showed a continuous linear increase without convergence after approximately 7 minutes from the onset of exposure. This suggests that paired implant placement may facilitate localized RF energy concentration, implying that local thermal safety may vary depending on the structural configuration of the implants, even in a 3T environment.

In the 11.74T ultra-high-field MRI environment, a significantly greater temperature rise than at 3T was observed across all cases. The thermal distribution simulation results showed a rapid temperature rise immediately after the onset of exposure in the 11.74T environment, and the maximum temperature in the dental region exceeded 46 °C across all cases after 15 minutes of

exposure. Temperatures above 46 °C represent a hazardous level at which cell necrosis and permanent tissue damage may occur, clearly exceeding the permissible limits from a biosafety perspective. In particular, unlike the convergence trend observed in the 3T environment, a pattern of linearly increasing temperature without convergence was observed in the 11.74T environment, even at the end of the 15-minute exposure period. This indicates that the rate of heat generation exceeds the heat dissipation and diffusion capacity of biological tissues, suggesting that the risk of thermal damage may increase even more sharply with increasing exposure time.

Regarding the mechanisms underlying these distinct thermal patterns, in Cases 4 and 5 of 3T, the relatively lower peak temperature but sustained linear increase, compared to the logarithmic convergence observed in Cases 1, 2, and 3, suggests a difference in the underlying heat transfer dynamics. One possible explanation is that the opposing implant geometry may alter the spatial distribution of RF-induced heating from a localized point source to a more distributed pattern within the inter-implant region. Additionally, the presence of metallic surfaces on both sides of the heated tissue could partially restrict thermal dissipation pathways, potentially delaying the establishment of thermal equilibrium beyond the 15-minute simulation period. However, further investigation would be needed to fully elucidate this mechanism. In the 11.74T environment, the maximum temperature in the dental region exceeded 46 °C after 15 minutes and exhibited a linear increase over time across all cases, regardless of implant configuration. This may be attributed to the substantially higher RF power required to reach the wbSAR safety limit, resulting in a heat generation rate that potentially exceeds the tissue's thermal dissipation capacity throughout the entire simulation period.

Meanwhile, because the power applied in the 3T and 11.74T thermal simulations in this study was limited based on the permissible limit of wbSAR, if the power had been set based on the permissible limits of the local SAR criterion $psSAR_{10g}$ or the hdSAR, the applied power would be considerably lower than in this study, and the magnitude of temperature rise would be expected to decrease further beyond the results of this study. Nevertheless, the overall temperature differences among cases according to implant location and quantity were minor compared with the implant-free case. This indicates that, despite the increase in field strength, the presence and placement of dental implants do not function as independent risk factors driving the average temperature rise across the entire head.

In this study, it should be noted that the findings are limited to the specific conditions modeled herein, namely, a single titanium dental implant geometry, a fixed implant orientation, and the Duke human body model. The observation that the implant did not produce a clinically significant increase in overall SAR or thermal burden should not be extrapolated to other implant types, sizes, materials, orientations, or patient anatomies without further validation. Additionally, because the RF coils used at 3T and 11.74T differ in structure, size, and operating principle, the absolute numerical SAR values may vary with factors such as coil tuning and matching conditions; however, the comparative trends observed between the two field strengths under matched $|B_1^+|$ conditions are expected to remain valid. The thermal simulations also assumed a fixed blood perfusion rate; if thermoregulatory responses were incorporated, different temperature elevation patterns might be observed. Therefore, future studies should employ multiple human body models with varying anatomies, investigate a broader range of implant geometries, sizes, materials, and orientations, and incorporate physiological thermoregulation to further assess the generalizability of the present findings.

5. Conclusion

This study systematically evaluated the RF-induced thermal effects of dental implants in 3T and 11.74T MRI environments through numerical simulations. In the 3T environment, the presence of dental implants did not significantly increase the average thermal load across the head, although localized temperature elevations near the implants approached biologically relevant thresholds. In the 11.74T environment, all cases exhibited temperature increases exceeding safety thresholds regardless of implant configuration, indicating that RF power level, rather than implant presence, is the dominant factor governing thermal risk at ultra-high field strengths. These results suggest that while dental implants may be considered MR Conditional under current 3T safety guidelines, additional safety measures or exposure limitations may be necessary for ultra-high-field MRI applications.

Funding

This work was supported by the National Research Foundation of Korea (NRF) grant funded by the Korean Government (MSIT) (RS-2025-23523111).

References

[1] V. P. Grover, J. M. Tognarelli, M. M. Crossey, I. J. Cox,

S. D. Taylor-Robinson, and M. J. McPhail, J. Clin. Exp. Hepatol. **5**, 246 (2015).
[2] S. Lim and Y. Lee, Med. Phys. **53**, e70379 (2026).
[3] K. Kim, C. Park, and Y. Lee, Journal of Magnetics **29**, 237 (2024).
[4] S. H. Kang, J. Y. Chung, and Y. Lee, Magnetochemistry **12**, 14 (2026).
[5] A. J. Fagan, A. K. Bitz, I. M. Björkman-Burtscher, C. M. Collins, V. Kimbrell, and A. J. E. Raaijmakers, J. Magn. Reson. Imaging **53**, 333 (2020).
[6] G. Barisano, F. Sepehrband, S. Ma, K. Jann, R. Cabeen, D. J. Wang, A. W. Toga, and M. Law, Br. J. Radiol. **92**, 20180492 (2019).
[7] E. Moser, E. Laistler, F. Schmitt, and G. Kontaxis, Front. Phys. **5**, 1 (2017).
[8] E. Yacoub, A. Shmuel, J. Pfeuffer, P. F. Van De Moortele, G. Adriany, P. Andersen, J. T. Vaughan, H. Merkle, K. Ugurbil, and X. Hu, Magn. Reson. Med. **45**, 588 (2001).
[9] M. K. Akter, A. Shen, M. Z. Islam, L. Zhang, J. Zheng, and J. Chen, Magn. Reson. Med. **94**, 2632 (2025).
[10] S. Tsutsui, T. Matsuda, K. Takeda, M. Sasaki, Y. Kubo, K. Setta, S. Fujiwara, K. Chida, and K. Ogasawara, AJNR Am. J. Neuroradiol. **43**, 972 (2022).
[11] Y. Noureddine, O. Kraff, M. E. Ladd, K. Wrede, B. Chen, H. H. Quick, G. Schaefers, and A. K. Bitz, Magn. Reson. Med. **82**, 1859 (2019).
[12] M. Hasegawa, K. Miyata, Y. Abe, T. Ishii, T. Ishigami, K. Ohtani, E. Nagai, T. Ohyama, Y. Umekawa, and S. Nakabayashi, Dentomaxillofac. Radiol. **44**, 20150011 (2015).
[13] R. Guo, J. Zheng, Y. Wang, Q. Zeng, Q. Wang, R. Yang, W. Kainz, and J. Chen, Magn. Reson. Med. **82**, 1848 (2019).
[14] L. Winter, F. Seifert, L. Zilberti, M. Murbach, and B. Ittermann, J. Magn. Reson. Imaging **53**, 1646 (2021).
[15] ASTM International, ASTM Standard F2182-19e2, West Conshohocken, PA (2019).
[16] E. Kazemivalipour, B. Guerin, and L. L. Wald, Magn. Reson. Med. **94**, 835 (2025).
[17] D. Hernandez and K. N. Kim, Investig. Magn. Reson. Imaging **24**, 95 (2020).
[18] M. C. Gosselin, E. Neufeld, H. Moser, E. Huber, S. Farcito, L. Gerber, M. Jedensjö, I. Hilber, F. D. Gennaro, B. Lloyd, E. Cherubini, D. Szczerba, W. Kainz, and N. Kuster, Phys. Med. Biol. **59**, 5287 (2014).
[19] International Electrotechnical Commission, IEC 60601-2-33 Ed. 3.0 (2010).
[20] S. J. Malik, J. Hand, D. W. Carmichael, and J. V. Hajnal, Magn. Reson. Med. **88**, 1434 (2022).